

Analytical model for gravity segregation of horizontal multiphase flow in porous media

Cite as: *Phys. Fluids* **32**, 046602 (2020); doi: [10.1063/5.0003325](https://doi.org/10.1063/5.0003325)

Submitted: 1 February 2020 • Accepted: 17 March 2020 •

Published Online: 9 April 2020



View Online



Export Citation



CrossMark

Avinoam Rabinovich,^{1,a)}  Pavel Bedrikovetsky,² and Daniel M. Tartakovsky³ 

AFFILIATIONS

¹School of Mechanical Engineering, Tel-Aviv University, Tel-Aviv 69978, Israel

²Australian School of Petroleum, University of Adelaide, South Australia 5005, Australia

³Department of Energy Resources Engineering, Stanford University, Stanford, California 94305, USA

^{a)} Author to whom correspondence should be addressed: avinoamr@tauex.tau.ac.il

ABSTRACT

Simultaneous horizontal injection of two immiscible fluids into a porous medium gives rise to three regions of constant saturation. Due to gravity impact, the region with fluid saturation reflecting the volume fraction and viscosity ratio of the injected fluids morphs into two horizontal layers fully saturated with one fluid or the other. The location of the discontinuity separating constant saturation regions is often estimated with the Stone–Jenkins (SJ) formula. Our numerical simulations of multiphase flow in porous media demonstrate that, for a wide range of hydraulic parameters of practical significance, the SJ formula has substantial error. We derive an approximate analytical solution, which neglects the vertical component of flow velocity and introduces a correction factor to enforce mass conservation. Comparison with numerical simulations reveals that our solution is accurate in the parameter regimes for which the SJ formula is not and vice versa. The two solutions are complementary, covering the entire range of physically realizable parameters.

Published under license by AIP Publishing. <https://doi.org/10.1063/5.0003325>

I. INTRODUCTION

Segregation of fluids in porous media plays an important role in a plethora of applications, which range from volcanology¹ and petroleum geology² to metallurgy³ and cell biology.⁴ Despite the superficial similarity between these phenomena, the mechanisms leading to fluid segregation are application-specific. We focus on the effects of gravity on flow and segregation of two immiscible fluids in a porous medium.

Macroscopic models of multiphase flow in porous media rely on a coupled system of highly nonlinear parabolic equations, which describe the spatiotemporal evolution of saturations of individual phases. Except in a few special cases, the solution of these equations requires sophisticated numerical algorithms,^{5,6} often employing computationally intense commercial simulators. One such case is steady-state horizontal two-phase flow in a homogeneous medium with negligible capillary forces. When gravitation and viscous forces

are of the same order of magnitude and considering certain domain geometries with a boundary condition of uniform injection, resulting flows are two-dimensional. This flow regime is observed in a number of porous media applications such as water-alternating-gas enhanced oil recovery,^{7,8} foam injection into oil reservoirs,^{9–11} CO₂-oil coreflooding,¹² and CO₂-water coreflooding¹³ related to CO₂ sequestration.^{14,15} Impact of gravity on horizontal multiphase flow is important in many coreflooding experiments, e.g., in drainage by N₂ or CO₂, wherein it can alter the estimation of core relative permeability.^{13,16}

Several previous investigations focused on gravity segregation of steady-state horizontal multiphase flow in homogeneous porous media. A heuristic analytical expression, first derived by Stone⁷ and Jenkins (SJ)⁸ and henceforth referred to as the SJ formula, posits that a flow domain consists of three constant-saturation regions separated by discontinuities. This approximate expression has been shown to agree with numerical simulations under certain conditions

and proved to be useful in applications.^{17–19} Yet, its heuristic nature, i.e., the lack of rigorous derivation of the SJ formula, precludes one from both quantifying its predictive error and identifying the limits of its applicability. Analyses by Rossen and Van Duijn⁹ and Rossen *et al.*²⁰ demonstrated that the SJ formula predicts exactly the distance at which full segregation occurs. However, these studies left unexplored the shape of the boundaries between the three saturation regions and, more specifically, its conformance with full numerical simulations.

We present an approximate analytical solution to gravity segregation in steady-state, two-dimensional, immiscible two-phase, horizontal flow. This solution is derived by assuming that the vertical component of total flow velocity is negligible, i.e., that the sum of wetting- and nonwetting-phase vertical velocities is much smaller than the total horizontal velocity. A similar approximation was used by Zhou *et al.*²¹ (Sec. II A) in the context of gravity-dominated crossflow to classify flow regions without solving any specific flow problem. Kuo and Benson¹³ neglected the total vertical velocity to derive a semi-empirical model of gravity–capillary–viscous flow; their solution involves a number of fitting parameters, which are obtained by matching numerical simulations. To the best of our knowledge, the assumption of zero total vertical velocity has not yet been rigorously implemented to solve flow problems of horizontal two- or three-dimensional flows in the presence of gravity.

Our analysis starts by invoking the assumption of negligible total vertical velocity to simplify the governing equations. Then, we analyze this approximation and show that it only applies to the unlikely case of isoviscous fluids, contradicting mass conservation when phase viscosities are unequal. Hence, the solution necessitates introducing a correction term. This finding is important due to its implications on past and future investigations employing this approximation. The resulting governing equations for the two-dimensional saturation distribution are solved by using the method of characteristics. The solution describes the distance and depth at which full segregation occurs. These predictions are in agreement with previous publications; however, unlike existing literature, our solution also predicts the shape of the boundaries separating the three constant saturation regions.

The second part of our study provides a comparison between our solution, the SJ formula, and a direct numerical solution of the multiphase flow equations. This comparison establishes the limits of applicability of the two analytical solutions. It shows that for a wide range of parameters, our analytical solution is more accurate than the SJ formula. We identify threshold values of the hydraulic parameters for which the SJ formula is more accurate than ours. For example, the SJ formula should be used when the dimensionless gravity number is small, while beyond a certain threshold value of this number, our analytical solution is more accurate.

In Sec. II, we formulate the governing equations and boundary conditions using dimensionless parameters. Section III contains an analysis of the new approximation and discusses its failure to honor mass conservation. In Sec. IV, we derive an analytical solution to the problem, formulated with a correction that ensures mass conservation. In Sec. V, numerical results for saturation are presented for a wide range of parameters and compared with the analytical and

SJ solutions. Section VI provides an analogous solution in cylindrical coordinates. Finally, in Sec. VII, we provide a summary of our findings and list major conclusions.

II. PROBLEM FORMULATION

We consider horizontal flow in a homogeneous porous medium due to the simultaneous injection of two immiscible fluids. Both the porous medium and fluids are assumed to be incompressible and the medium’s permeability to be isotropic. The flow is described by the continuity and Darcy equations,

$$\phi \frac{\partial S_j}{\partial t} + \nabla \cdot \mathbf{u}_j = 0 \tag{1}$$

and

$$\mathbf{u}_j = - \frac{kk_{rj}(S_w)}{\mu_j} \nabla (p_j + \rho_j g z), \tag{2}$$

where ϕ is the porosity of the rock, S_j is the saturation of phase j ($j = w$ for wetting phase and $j = nw$ for nonwetting phase), \mathbf{u}_j is the velocity vector of phase j , k_{rj} is the relative permeability to phase j , μ_j is the viscosity of phase j , k is the absolute permeability, p_j is the pressure of phase j , ρ_j is the phase density, g is the gravitational acceleration, and z is the vertical coordinate. The saturations satisfy the constraint $S_w + S_{nw} = 1$, and assuming negligible capillary pressure, the wetting and nonwetting phase pressures are equal, $p_w = p_{nw} = p$. The problem formulation is completed by specifying functional forms of the constitutive laws $k_{rj} = k_{rj}(S_w)$.

The flow domain is a parallelepiped ($0 \leq x \leq L$, $0 \leq y \leq L$, and $0 \leq z \leq H$), with injection of fluids at one of its faces ($x = 0$) and extraction at the opposite face ($x = L$). Since permeability is assumed to be isotropic and homogeneous ($k_x = k_y = k_z = \text{const}$), this flow regime is two-dimensional (in the $\{x, z\}$ Cartesian coordinate system). The steady-state flow regime is described by the combination of (1) and (2) without the time derivative,

$$\nabla \cdot [k_{rj}(S_w) \cdot \nabla (p + \rho_j g z)] = 0. \tag{3}$$

The boundary conditions of the problem are a given x -direction Darcy velocity for each phase at the inlet,

$$u_j = - \frac{kk_{rj}}{\mu_j} \frac{\partial p}{\partial x} = U_j, \quad x = 0, \tag{4}$$

no perpendicular flow at the top and bottom boundaries,

$$\frac{\partial p}{\partial z} = 0, \quad z = 0 \text{ and } z = H, \tag{5}$$

and an open boundary at the outlet $x = L$. The injected velocity of phase j is denoted as U_j .

The two equations given by (3), together with the boundary conditions of Eqs. (4) and (5), form a system for the two unknowns $p(x, z)$ and $S_w(x, z)$. These can be applied to describe a number of processes related to injection of fluid mixtures into porous media, e.g., two-phase flow coreflooding experiments²² and enhanced oil recovery. The solution for spatial variation of pressure and saturation is generally a function of parameters $L, H, \mu_j, k_{rj}, U_j, k$, and

$\Delta\rho = \rho_w - \rho_{nw}$. Applying dimensional analysis using length scale L , time scale L/U , and mass $\mu_{nw}L^2/U$, where $U = U_w + U_{nw}$ is the total injection velocity, we arrive at dimensionless parameters. If we also assume Brooks–Corey²³ relative permeability functions of the form

$$k_{rw} = (1 - S_{nw})^n, \quad k_{rnw} = S_{nw}^n, \quad (6)$$

then six dimensionless parameters control the flow and these are

$$\begin{aligned} \mu_R &= \frac{\mu_w}{\mu_{nw}}, \quad R = \frac{H}{L}, \quad U_w^* = \frac{U_w}{U}, \\ \Delta\rho^* &= \frac{\Delta\rho g L^2}{\mu_{nw} U}, \quad K = \frac{k}{L^2} \quad \text{and} \quad n. \end{aligned} \quad (7)$$

To solve Eqs. (3)–(5), we will apply an approximation of the small total vertical velocity. The total velocity is defined by $\mathbf{u}^t = (u_x^t, u_z^t) = \mathbf{u}_w + \mathbf{u}_{nw}$, and from Eq. (1) at steady state, we obtain the relationship

$$\nabla \cdot \mathbf{u}^t = 0, \quad (8)$$

i.e., the flow is incompressible. The basic intuition for neglecting total vertical velocity, i.e.,

$$u_z^t \ll u_x^t, \quad (9)$$

comes from the fact that we impose flow in the horizontal direction. However, this approximation is only valid for some cases, which will be discussed in Sec. III.

Neglecting u_z^t in Eq. (8) immediately results in $u_x^t = \text{const} = U$. Using this result ($u_{w,x} + u_{nw,x} = U$) together with Darcy’s law, we write the following expressions for the nonwetting phase velocities:

$$u_{nw,x} = \frac{U}{1 + \lambda_w/\lambda_{nw}}, \quad (10)$$

$$u_{nw,z} = \frac{k\lambda_w\Delta\rho g}{1 + \lambda_w/\lambda_{nw}}, \quad (11)$$

where $\lambda_j = k_{rj}/\mu_j$ is the phase mobility. Substituting Eqs. (10) and (11) in the steady-state form of Eq. (1) for $j = nw$ gives

$$\frac{\partial}{\partial x} \left[\frac{U}{1 + M} \right] + \frac{\partial}{\partial z} \left[\Delta\rho g \frac{k\lambda_w}{1 + M} \right] = 0, \quad (12)$$

where $M = \lambda_w/\lambda_{nw}$.

We use the nondimensional parameters $\tilde{x} = x/L$ and $\tilde{z} = z/H$ in Eq. (12) and rearrange to arrive at the nondimensional equation,

$$\frac{\partial F_1}{\partial \tilde{x}} + \frac{\partial F_2}{\partial \tilde{z}} = 0, \quad (13)$$

where

$$F_1(S) = \frac{1}{1 + M}, \quad F_2(S) = N_g \frac{Mk_{rnw}}{1 + M}, \quad (14)$$

and $N_g = kL\Delta\rho g/(H\mu_{nw}U)$ is the gravity number representing the ratio of gravity to viscous forces. The saturation S in Eq. (14) is the nonwetting phase saturation normalized to incorporate residual saturations, i.e., $S = (S_{nw} - S_{wr})/(1 - S_{wr} - S_{nwr})$, where S_{wr} and S_{nwr} are the wetting/nonwetting phase residuals and S_{nw} is the nonwetting phase saturation. Equation (13) resembles the well-known Buckley–Leverett equation,²⁴ where time is replaced with \tilde{x} and reservoir length coordinate is replaced with \tilde{z} .

We seek the two-dimensional saturation solution $S(x, z)$ of the above problem, while pressure can be obtained once saturation is known via Eqs. (10) and (11) by applying Darcy’s law. The boundary conditions for saturation will be derived and these are depicted in Fig. 1. At the inlet boundary, saturation S_{in} is obtained by applying Eq. (10) at $\tilde{x} = 0$ and replacing the velocity $u_{nw,x}$ with the injection velocity U_{nw} . The resulting equation is

$$\frac{\lambda_w(S_{in})}{\lambda_w(S_{in}) + \lambda_{nw}(S_{in})} = \frac{k_{rw}(S_{in})}{k_{rw}(S_{in}) + \mu_R k_{rnw}(S_{in})} = U_w^*, \quad \tilde{x} = 0, \quad (15)$$

where $\mu_R = \mu_w/\mu_{nw}$ is the viscosity ratio and $U_w^* = U_w/U$. Equation (15) can be easily solved to obtain S_{in} , once the structure of relative permeability functions is determined [assumed here to be Eq. (6)]. At the top and bottom boundaries, Eq. (11) with the no flow condition suggests that

$$u_{nw,z} = -u_{w,z} = \frac{k\lambda_w\Delta\rho g}{1 + \lambda_w/\lambda_{nw}} = 0, \quad \tilde{z} = 0, 1. \quad (16)$$

Possible solutions are $\lambda_w = 0$ or $\lambda_{nw} \rightarrow 0$, corresponding to $S = 1$ and $S = 0$, respectively.

For a sufficiently large domain length L , the flow will become fully segregated at a certain distance from the inlet, denoted by x' (normalized by L), and the lighter phase will form a layer above the heavier phase (see Fig. 1). We denote by z' the dimensionless height (normalized by H) at which the two segregated phases are in contact. The point (x', z') is coined the segregation point. For demonstration purposes, we will assume that the nonwetting phase is lighter (e.g., gas) than the wetting phase (e.g., water). Hence, for $\tilde{x} > x'$, $S = 0$ at $\tilde{z} < z'$ and $S = 1$ at $\tilde{z} > z'$, i.e., the lighter phase is completely above the heavier phase. Therefore, we specify the top and bottom boundary conditions to be

$$S = 0 \quad \text{at} \quad \tilde{z} = 0, \quad S = 1 \quad \text{at} \quad \tilde{z} = 1. \quad (17)$$

These three boundary conditions given by Eqs. (15) and (17) (inlet, top and bottom) are sufficient to solve the problem.

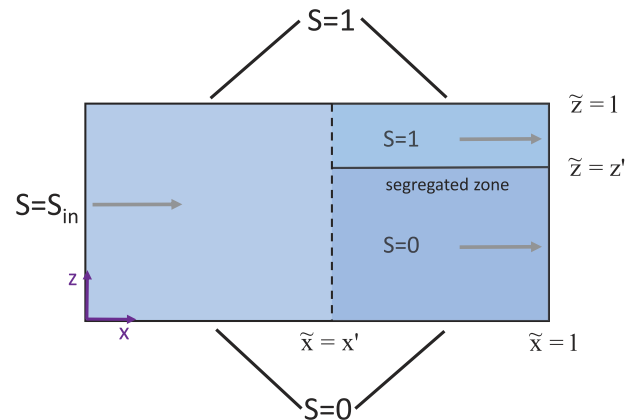


FIG. 1. Schematic description of the problem, including 2D domain, coordinate system, saturation boundary conditions, and segregation point (x', z') .

Nevertheless, we can also express the saturation at the segregation line as

$$\begin{aligned} S = 1 & \quad \text{at } \tilde{x} = x', \quad z' < \tilde{z} < 1, \\ S = 0 & \quad \text{at } \tilde{x} = x', \quad 0 < \tilde{z} < z'. \end{aligned} \tag{18}$$

Full segregation may not occur in the domain, i.e., when $x' > 1$; however, it will be shown that considering an imaginary segregation point (outside the domain) is useful in deriving a solution. The solution to the approximate equations given by Eqs. (13)–(15) and (17) is controlled by four parameters, i.e., μ_R , U_w^* , N_g , and n , two less than the full problem detailed in Eq. (7).

III. ANALYSIS OF APPROXIMATION

We now investigate the proposed approximation of negligible total vertical velocity [Eq. (9)]. The main goal is to assess its applicability and to determine the parameters for which the assumption is reasonable. First, we can test the approximation by considering the conservation of mass at the segregation line $\tilde{x} = x'$. Since flow is only in the x direction at both $x = 0$ and $\tilde{x} = x'$, we can write an equation of mass balance between the two lines for each phase as follows:

$$\int_{z'}^1 u_{nw,x} d\tilde{z} = U_{nw}, \tag{19a}$$

$$\int_0^{z'} u_{w,x} d\tilde{z} = U_w. \tag{19b}$$

Substituting Darcy's law in Eq. (19) and integrating it, we arrive at

$$(1 - z')\lambda_{nw} \frac{\partial p}{\partial x} = U_{nw}, \tag{20a}$$

$$z'\lambda_w \frac{\partial p}{\partial x} = U_w, \tag{20b}$$

which leads to an expression for the segregation height,

$$z' = \frac{1}{\frac{U_{nw}\mu_{nw}}{U_w\mu_w} + 1}. \tag{21}$$

On the other hand, we can obtain z' using the zero total vertical velocity assumption by substituting Eq. (10) in Eq. (19a), which after integration leads to

$$\frac{(1 - z')U}{1 + \lambda_w/\lambda_{nw}} = U_{nw}. \tag{22}$$

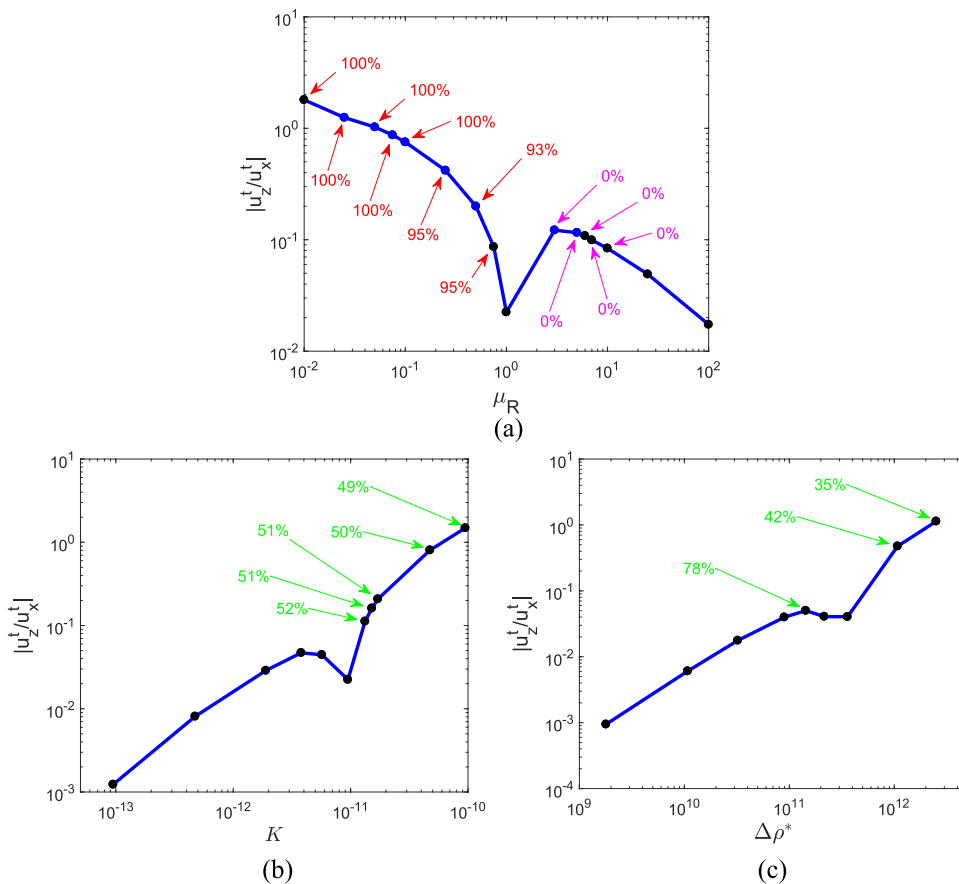


FIG. 2. Vertical to horizontal total velocity ratio averaged over the domain as a function of (a) viscosity ratio, (b) dimensionless permeability, and (c) dimensionless density difference. Arrows with percent values indicate the portion of grid blocks with negative (downward) vertical velocity.

Remembering that $\lambda_w = 0$ because $S_{nw} = 1$ in the region $z' < \tilde{z} < 1$ of the segregated zone, we arrive at

$$z' = \frac{1}{U_{nw}/U_w + 1}. \tag{23}$$

This result for z' is clearly different than the previous one in Eq. (21) known to be correct. It shows that the approximation does not incorporate the effects of the viscosity ratio in the fully segregated flow. An additional, mathematically rigorous proof of the incompatibility between the approximate and full equations is presented in the Appendix. The reason for the failure of the approximation will be discussed in the next paragraphs; however, it is important to stress the implications of this finding. Noncompliance with basic mass balance is a major problem and puts in question the previous and future applications of the zero total vertical velocity assumption. In this work, we will overcome this issue by applying a correction, which will be discussed in Sec. IV.

Next, we test the approximation by calculating u'_z using numerical solutions. The full problem, given by Eqs. (1) and (2), is solved using Stanford's General Purpose Research Simulator (GPRS²⁵) on simulation grids of 200×200 until steady state is reached. The ratio between total vertical and horizontal velocities, i.e., $|u'_z/u'_x|$, is calculated in each grid block and we generally expect this ratio to be small when the approximation applies. Figures 2(a)–2(c) present the velocity ratio averaged over the domain in the region $0 < \tilde{x} < x'$, $0 < \tilde{z} < 1$ for changing viscosity ratio (μ_R), dimensionless permeability $K = k/L^2$, and density difference $\Delta\rho^* = \Delta\rho g L^2 / (\mu_{nw} U)$.

Figure 2(a) reveals that away from $\mu_R = 1$, there is a jump in the velocity ratio, indicating inadequacy of the approximation and in line with our previous finding that mass conservation fails for $\mu_R \neq 1$. This non-negligible vertical velocity, resulting from the viscosity difference between the phases, leads to a shift in z' , as the more viscous phase will occupy a thicker layer in segregated flow. This is seen in Fig. 2(a), where each data point is accompanied by an arrow indicating the percent of grid blocks that have downward direction velocity (i.e., $u'_z < 0$). It is clear that for $\mu_R < 1$, almost all the non-negligible vertical velocity is downward, while for $\mu_R > 1$, it is all upward. This corresponds to the decrease in z' for the former and increase for the latter [see Eq. (21)]. Points in the plot that have no indicated percentage pertain to cases with small vertical velocity (less than 10% of grid blocks with $|u'_z/u'_x| > 0.1$) so that the direction is immaterial. Comparison with the vertical velocity direction in Figs. 2(b) and 2(c) shows that the direction is significantly more mixed between upward and downward and is not associated with a change in z' .

Despite the local increase in $|u'_z/u'_x|$ away from $\mu_R = 1$, a strong decrease is seen in Fig. 2(a) for large μ_R . This is a result of the solution approaching one of constant saturation with only horizontal flow and a segregation point that is far outside the domain ($x' \gg 1$). The same phenomenon occurs for small K and $\Delta\rho^*$ in Figs. 2(b) and 2(c), respectively. This decrease is associated with a smaller gravity number, which, in fact, leads to a constant saturation solution as gravity effects become negligible. A larger gravity number, i.e., increasing K and $\Delta\rho^*$, leads to more segregated solutions in which only a small region near the inlet consists of mixed phases. Figures 2(b) and 2(c) show that these solutions have increasingly large vertical velocities, which must be attributed to near inlet regions.

IV. SOLUTION

We now derive an analytical solution to the approximate problem given by Eqs. (13)–(15) and (17). The solution is obtained using the method of characteristics, following the approach detailed in the work of Bedrikovetsky.²⁶ Rewriting Eq. (13) as

$$\frac{\partial S}{\partial \tilde{x}} + F' \frac{\partial S}{\partial \tilde{z}} = 0, \tag{24}$$

where

$$F'(S) = \frac{\partial F_2}{\partial S} / \frac{\partial F_1}{\partial S}, \tag{25}$$

allows us to define the slope of the characteristic curves, $d\tilde{z}/d\tilde{x} = F'(S)$. Assuming Brooks–Corey relative permeability functions in Eq. (6), F'/N_g is a function only of n and μ_R . We plot $\tilde{F} = F'/N_g$ for varying n and μ_R in Figs. 3(a) and 3(b). Characteristic lines are determined by \tilde{F} at $S = 0$, $S = 1$, and $S = S_{in}$, corresponding to the lines originating from the bottom, top, and inlet.

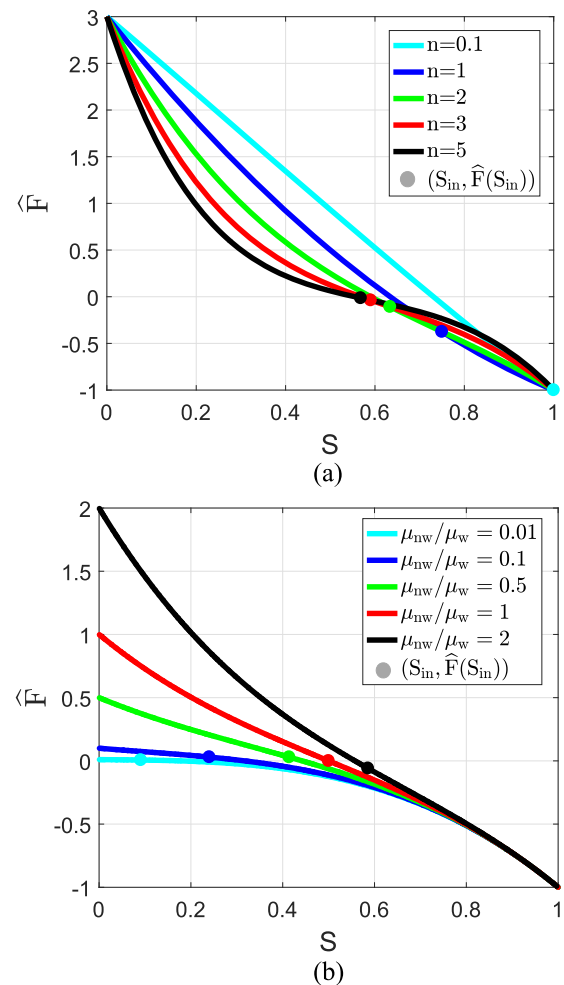


FIG. 3. $\tilde{F} = F'/N_g$ [Eq. (25)] as a function of S for (a) varying n and (b) varying μ_R . The points $(S_{in}, \tilde{F}(S_{in}))$ are indicated with filled circles.

Figures 3(a) and 3(b) show that for all μ_R and n values, $F' = -1$ at $S = 1$, and therefore, all characteristic curves from the top boundary will be 45° to the x axis (for $N_g = 1$). This can be seen in Fig. 4 where the characteristics for the case of $N_g = 1$, $n = 2$, and $\mu_{nw}/\mu_w = 1$ are drawn. On the other hand, curves from the bottom of the domain will have gradients varying with μ_{nw}/μ_w , but not n , as determined by $F'(0)$. Curves at the inlet will vary with n and slightly with μ_R , determined by $F'(S_{in})$. These curves also depend on U_w^* (taken to be unity in the figures), since the injection velocities impact S_{in} , as seen in Eq. (15). Figure 4 presents characteristic curves of the problem for an example case. It can be seen that top and bottom curves are $\pm 45^\circ$ from the horizontal and the inlet curves are parallel to \tilde{x} axis. This corresponds to $\tilde{F}'(0) = 1$, $\tilde{F}'(1) = -1$, and $\tilde{F}'(S_{in}) = 0$, as seen in Fig. 3(b) for $\mu_R = 1$. The characteristic curves show that the solution consists of three regions of constant saturation, $S = 1$, $S = 0$, and $S = S_{in}$, separated by three shock waves, i.e., discontinuities. Furthermore, the whole domain is covered by characteristics indicating that there are no rarefaction waves and the Lax²⁷ condition holds. This is the case for any choice of parameters μ_R , n , U_w^* , and N_g , as shown in Figs. 3(a) and 3(b).

To complete the solution, it is necessary to find equations describing the discontinuity lines separating the three regions of constant saturation. For this, we apply the Rankine–Hugoniot²⁸ condition and obtain the line gradients, often termed “velocity of the waves.” A simple wave solution is assumed, i.e., $\zeta = \tilde{z} - D_i \tilde{x}$ ($i = 1, 2, 3$), where D_1 describes the gradient of the discontinuity beginning at the lower boundary, D_2 begins at the upper boundary, and D_3 is the angle of the segregation boundary at $\tilde{z} = z'$. Plugging the transformation into Eq. (13), integrating, and rearranging give an expression for D as follows:

$$D = \frac{F_2(S^+) - F_2(S^-)}{F_1(S^+) - F_1(S^-)}, \quad (26)$$

where S^+ and S^- are the saturation above and below the discontinuity, respectively. Then D for each discontinuity is

$$D_1 = \frac{F_2(S_{in}) - F_2(0)}{F_1(S_{in}) - F_1(0)} = \frac{F_2(S_{in})}{F_1(S_{in})}, \quad (27)$$

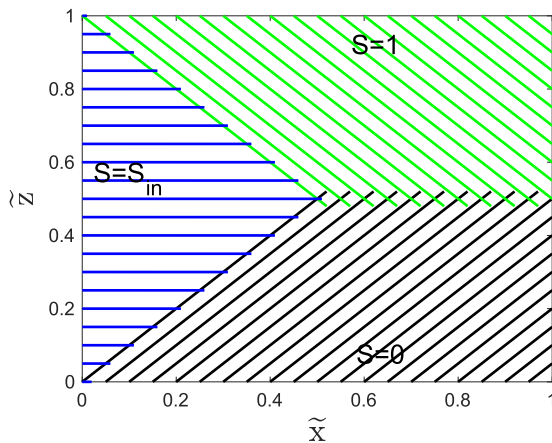


FIG. 4. Characteristic lines for the problem given by Eqs. (13)–(15) and (17). Parameter values of $N_g = 1$, $\mu_R = 1$, $U_w^* = 1$, and $n = 2$ are taken.

$$D_2 = \frac{F_2(1) - F_2(S_{in})}{F_1(1) - F_1(S_{in})} = \frac{-F_2(S_{in})}{1 - F_1(S_{in})}, \quad (28)$$

$$D_3 = \frac{F_2(1) - F_2(0)}{F_1(1) - F_1(0)} = 0, \quad (29)$$

where we have substituted $F_1(0) = 0$, $F_1(1) = 1$, $F_2(0) = 0$, and $F_2(1) = 0$ [see Eq. (14)]. As expected, the line in the segregated zone is simply horizontal, i.e., $D_3 = 0$.

The location of the segregation point (x', z') can be found by the relationship $D_1 x' = 1 + D_2 z'$, leading to

$$x' = \frac{1}{D_1 - D_2}, \quad z' = \frac{D_1}{D_1 - D_2}. \quad (30)$$

Substituting Eqs. (27) and (28) in (30) gives $z' = 1 - F_1(S_{in}) = 1/[1 + \lambda_w(S_{in})/\lambda_{nw}(S_{in})]$. Using Eq. (15), it is obvious that this expression for z' is consistent with mass conservation at the outlet boundary given by Eq. (23). As discussed previously in Sec. III, this expression is only correct when $\mu_R = 1$ and the correct expression is given by Eq. (21). Therefore, the discontinuity described by Eqs. (27) and (28) does not always honor mass conservation. However, this solution also leads to the horizontal coordinate of segregation by substitution in Eq. (30), which is now given by

$$x' = \frac{F_1(S_{in})[1 - F_1(S_{in})]}{F_2(S_{in})} = \frac{F_1(S_{in})}{N_g k_{rmw}(S_{in})}, \quad (31)$$

and this is accurate for any choice of parameters, as shown previously by Rossen and Duijn,⁹ Stone,⁷ and Jenkins,⁸ and will be shown here in Sec. V.

We now apply a correction to the solution for D_1 and D_2 so that the intersection of the discontinuity lines will remain at distance $\tilde{x} = x'$, yet the height of intersection z' is corrected to be that of Eq. (21). This is ensured by defining $\tilde{D}_1 = z'/x'$ and $\tilde{D}_2 = (z' - 1)/z'$ (since the shock lines are $\tilde{z} = \tilde{D}_1 \tilde{x}$ and $\tilde{z} = 1 + \tilde{D}_2 \tilde{x}$). Substituting Eqs. (21) and (31) in these expressions gives the final result for discontinuity gradients,

$$\begin{aligned} \tilde{D}_1 &= \frac{z' N_g k_{rmw}(S_{in})}{F_1(S_{in})} \\ &= N_g k_{rmw}(S_{in}) \left(\frac{1}{1 - U_w^*} \right) \left[\frac{1}{\mu_R} \left(\frac{1}{U_w^*} - 1 \right) + 1 \right]^{-1}, \end{aligned} \quad (32)$$

$$\tilde{D}_2 = \frac{(z' - 1) N_g k_{rmw}(S_{in})}{F_1(S_{in})} = -N_g k_{rmw}(S_{in}) [U_w^* (\mu_R - 1) + 1]^{-1}. \quad (33)$$

The final solution in the nondimensional form can be written as

$$S(\tilde{x}, \tilde{z}) = \begin{cases} 0, & \{\tilde{x} < x' \text{ and } \tilde{z}/\tilde{x} < \tilde{D}_1\} \text{ or } \{\tilde{x} > x' \text{ and } \tilde{z} < z'\} \\ S_{in}, & \{\tilde{z}/\tilde{x} > \tilde{D}_1 \text{ and } (\tilde{z} - 1)/\tilde{x} < \tilde{D}_2\} \\ 1, & \{\tilde{x} < x' \text{ and } (\tilde{z} - 1)/\tilde{x} > \tilde{D}_2\} \text{ or } \{\tilde{x} > x' \text{ and } \tilde{z} > z'\}. \end{cases} \quad (34)$$

V. RESULTS

The solution derived in Sec. IV will now be analyzed for a wide range of controlling parameters. A comparison will be held with a numerical solution of the full problem (3) using GPRS, as described in Sec. III. We emphasize that simulation results have been tested carefully for convergence. The following “base case” parameters are defined: $\mu_R = 1$, $n = 2$, $R = 2.18$, $K = 9.5 \cdot 10^{-12}$, and $\Delta\rho^* = 3.23 \cdot 10^{11}$, chosen so that the solution has significant S variation, i.e., (x', z') is near the domain center. These values will be used in the tests that follow, usually changing one or two of the parameters at a time. Furthermore, we will compare the analytical solution with a previous formula suggested by Stone⁷ and Jenkins⁸ (which we have referred to as the SJ formula),

$$\tilde{z}_u(\tilde{x}) = \left[1 - \frac{1 - x'/\tilde{x}}{k_{rw}(S_{in})} \right] \left[1 + \frac{1}{\mu_R} \left(\frac{1}{U_w^*} - 1 \right) - \frac{1 - x'/\tilde{x}}{k_{rw}(S_{in})} \right]^{-1}, \quad (35a)$$

$$\tilde{z}_l(\tilde{x}) = \left[1 + \frac{1}{\mu_R} \left(\frac{1}{U_w^*} - 1 \right) - \frac{1 - x'/\tilde{x}}{k_{rw}(S_{in})} \right]^{-1}, \quad (35b)$$

for the upper and lower discontinuities, respectively, where x' is given by Eq. (31). These two discontinuity curves honor the boundary conditions and conservation of mass [Eq. (21)], i.e., $\tilde{z}_u = 1, \tilde{z}_l = 0$ at $\tilde{x} = 0$, and $\tilde{z}_u = \tilde{z}_l = z'$ at $\tilde{x} = x'$.

Figure 5 presents the solution $S(\tilde{x}, \tilde{z})$ for different values of N_g , as indicated below each plot. Base case parameters are considered apart from $U_w^* = 2/3$ and varying $\Delta\rho^*$. It can be seen that the solution consists of three regions of constant saturation: $S = S_{in}$, $S = 0$, and $S = 1$ as discussed previously in the results for characteristic lines (Fig. 4). The meeting point of the three regions is the segregation point (x', z') , and it is apparent that the analytical results for this point (intersection of red solid lines) given by Eqs. (21) and (31) are in agreement with the numerical results. This is presented quantitatively in Table I, where it can be seen that values of S_{in} , x' , and z' match almost perfectly for all cases in this figure and the following figures as well. Missing values in the table are for cases in which a segregation point does not exist in the domain, e.g., Fig. 5(d).

The impact of N_g on the saturation solution is seen in Fig. 5. For large values [Fig. 5(a)], gravity dominates, and the domain consists almost entirely of segregated flow and the transition zone

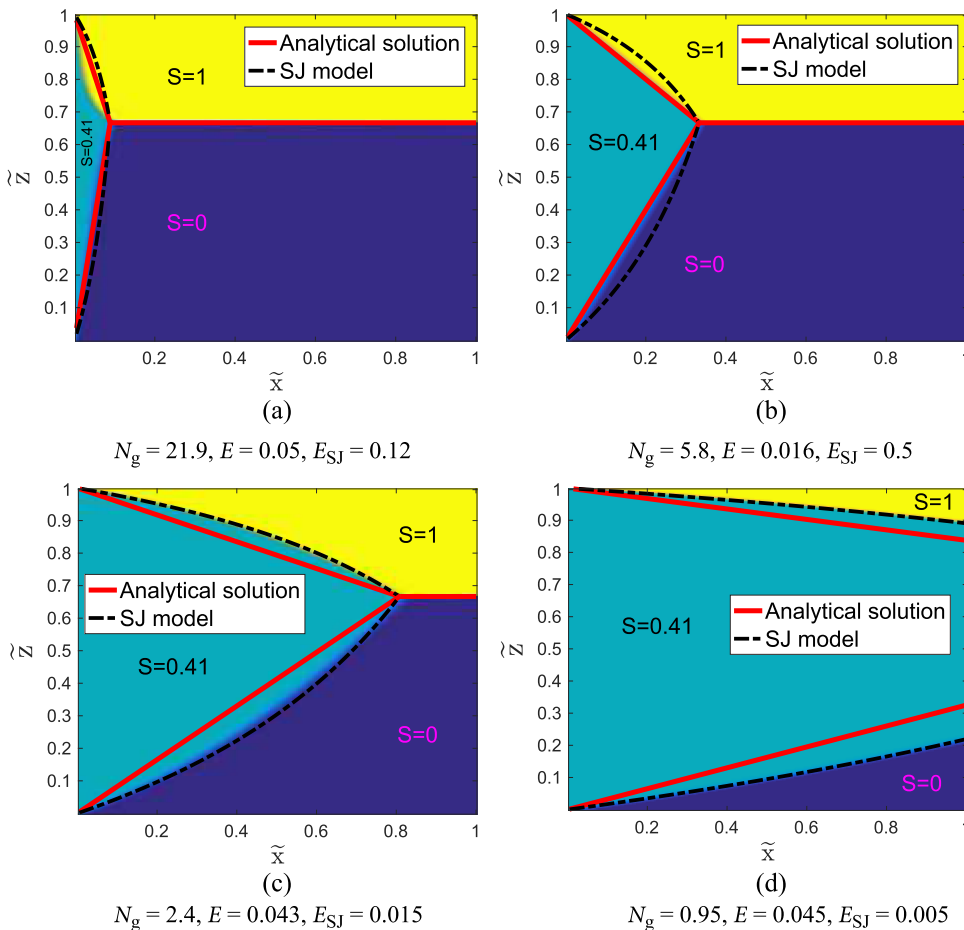


FIG. 5. Two-dimensional saturation solution for numerical simulations (colored areas), analytical solution, and the SJ formula. Different values of N_g are considered, as indicated below plots (a)–(d). Errors between numerical results and the analytical solution (E) or the SJ model (E_{SJ}) are detailed.

TABLE I. Values of S_{in} , x' , and z' for both the analytical and numerical solutions. Results pertain to the cases in Figs. 5–7.

Figure	S_{in}		x'		z'	
	Analytical	Numerical	Analytical	Numerical	Analytical	Numerical
5(a)	0.41	0.41	0.133	0.135	0.67	0.67
5(b)	0.41	0.41	0.33	0.34	0.67	0.66
5(c)	0.41	0.41	0.808	0.81	0.67	0.66
5(d)	0.41	0.41
6(a)	0.68	0.68	0.162	0.165	0.18	0.18
6(b)	0.53	0.53	0.269	0.27	0.44	0.44
6(c)	0.31	0.31	0.785	0.785	0.83	0.83
6(d)	0.24	0.24
7(a)	0.25	0.25	0.24	0.25	0.9	0.9
7(b)	0.5	0.5	0.114	0.115	0.5	0.5
7(c)	0.5	0.5	0.3	0.3	0.5	0.5
7(d)	0.75	0.75	0.25	0.25	0.1	0.1
7(e)	0.5	0.5	0.849	0.855	0.5	0.51

with $S = S_{in}$ is in a small region near the inlet. The decrease in N_g [Figs. 5(b) and 5(c)] leads to larger x' as the transition zone expands due to the increase in viscous effects. When viscous forces dominate [Fig. 5(d)], segregated flow does not occur and only small regions at the top and bottom of the domain have $S = 1$ and $S = 0$, respectively. These regions tend to zero with $N_g \rightarrow 0$, and the solution becomes uniform with $S = S_{in}$. We note that N_g does not impact the segregation height z' or the transition zone saturation $S = S_{in}$, as seen in Eqs. (21) and (15).

Since the analytical solutions for S_{in} , x' , and z' are exact, accuracy will be determined by the discontinuity curves separating saturation regions. In general, these curves change shape from concave [Figs. 5(c) and 5(d), numerical results] to convex [Fig. 5(a), numerical results] for the upper curve and vice versa for the lower curve. The analytical solution consists of linear curves, while the SJ formula [Eq. (35)] is generally concave (for the upper curve). Therefore, Figs. 5(c) and 5(d) show high accuracy of the SJ formula (compared with numerical results) as both are concave. In Fig. 5(b), the analytical solution is seen to be accurate as the curves are linear, while the SJ model loses its accuracy. Figure 5(a) shows that both approximate solutions are not accurate due to the convex curve structure; however, the analytical solution seems to have less error. Below each plot in Figs. 5–7, we specify a measure for the accuracy of the approximate solutions (analytical and SJ) by comparison to the numerical results. The overall error is defined as the average difference in saturation, i.e.,

$$E = \left\langle \left| S^{\text{approx}}(\tilde{x}, \tilde{z}) - S^{\text{numerical}}(\tilde{x}, \tilde{z}) \right| \right\rangle, \quad \tilde{x} < x', \quad (36)$$

where S^{approx} is the saturation for the analytical solution (E) or the SJ model (E_{SJ}), $S^{\text{numerical}}$ is the numerical solution, and $\langle \rangle$ represents spatial averaging.

Figure 6 presents results for the varying viscosity ratio μ_R . For small values of μ_R [Fig. 6(a)], the wetting phase has a higher Darcy velocity due to a smaller viscosity, and thus, the layer of segregated wetting phase is seen to be much thinner than the nonwetting phase

layer [small z' in Eq. (21)]. As μ_R is increased, z' will increase accordingly, and when the nonwetting phase is more viscous than the wetting, it will also become the thinner layer of the two [Fig. 6(c)]. The viscosity ratio has an additional impact on the solution via Eq. (31) for x' . Larger μ_R results in a larger transition region, and this can be seen in Figs. 6(a)–6(d). This leads to a break in symmetry as seen by comparing Figs. 6(a) and 6(c), showing that the solution for a less viscous wetting (heavy) phase is different than the solution for a less viscous nonwetting (light) phase. Accuracy of the approximate solutions is similar to that discussed previously, with better accuracy of the analytical solution for small μ_R (small x'), while the SJ model is more accurate for larger μ_R (larger x').

The impact of U_w^* is shown in Figs. 7(a), 7(c), and 7(d). Larger U_w^* [Fig. 7(a)] leads to a thicker wetting phase layer in the segregated flow, and smaller U_w^* leads to a thinner layer [Fig. 7(d)]. Furthermore, it is apparent that the solution for $0 < U_w^* < 0.5$ is symmetric with that for $0.5 < U_w^* < 1$, seen by comparing Figs. 7(a) and 7(d). This is due to the fact that U_w^* does not influence x' , while it has a symmetric impact on z' , seen in Eq. (21). For this reason, the impact of U_w^* on the accuracy of the analytical solution is limited, since most of the error variations occur with changes in x' . Figures 7(b), 7(c), and 7(e) present results for varying n . The impact of n is slightly hidden since it appears in k_{rw} and k_{rnw} in Eq. (6), which then impacts x' . It is seen in the figures that x' increases with larger n , while z' is not affected by n variations. The shape of discontinuity curves and the related error in approximate solutions appears to vary in the same manner as discussed previously, with a convex shape for small n and a concave shape for large n . However, the change in shape is much more pronounced than that is observed in Figs. 5 and 6.

To further test the applicability and accuracy of the analytical solution and to compare with the SJ model, we plot the overall errors E and E_{SJ} , given by Eq. (36), as a function of the six parameters of the full problem: $\Delta\rho^*$, μ_R , R , U_w^* , K , and n . Results are presented in Fig. 8 using base case parameters apart from the varying

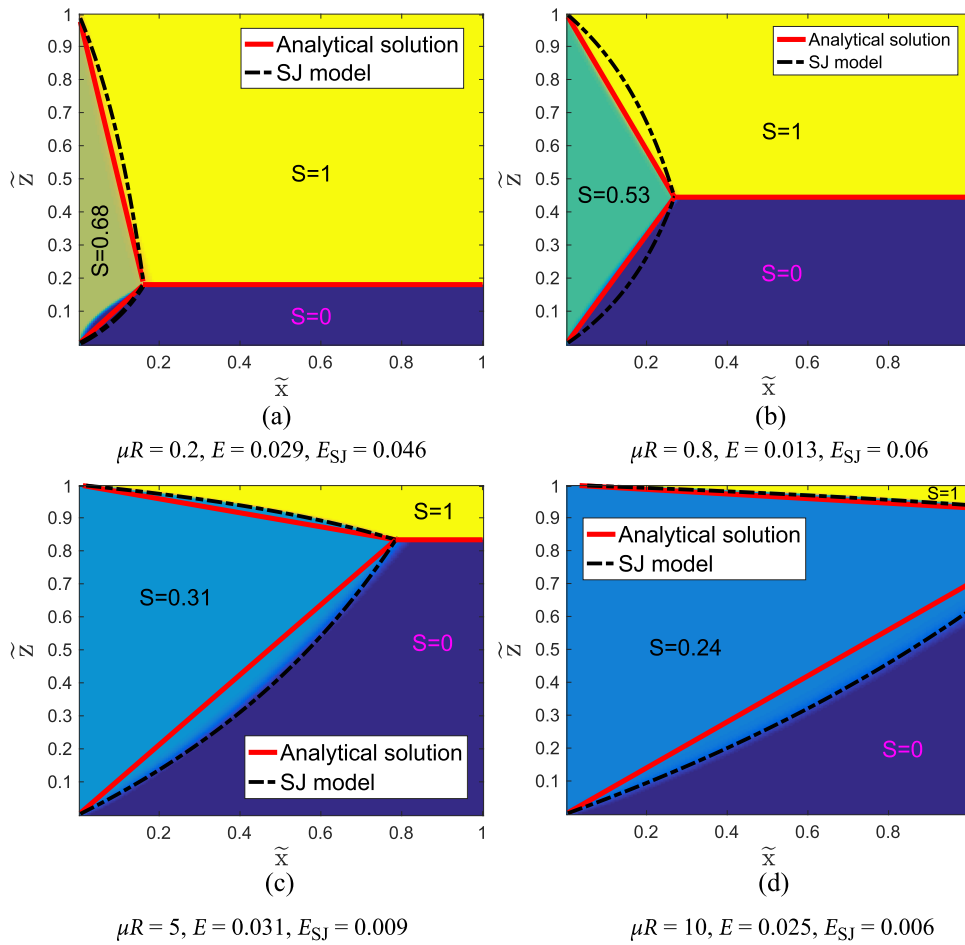


FIG. 6. Two-dimensional saturation solution for numerical simulations (colored areas), analytical solution, and the SJ formula. Different values of μR are considered, as indicated below plots (a)–(d). Errors between numerical results and the analytical solution (E) or the SJ model (E_{SJ}) are detailed.

parameter specified in the axes and $U_w^* = 2/3$ in Fig. 8(a). It is evident that the error curves in Figs. 8(a) and 8(e) have a very similar structure. Furthermore, E in Fig. 8(c) (red curve) also has a similar structure as those in Figs. 8(a) and 8(e) when considered backwards, i.e., from high to low values of R . This similarity is because the three parameters $\Delta\rho^*$, R , and K comprise the gravity number, i.e., $N_g = \Delta\rho^* K/R$, and their impact is rather similar when considered separately. This is the reason the analytical solution, which depends on N_g and not on the three parameters separately, is a useful approximation.

Observing the analytical solution and SJ model errors in Figs. 8(a), 8(c), and 8(e), we find that for small N_g (i.e., small $\Delta\rho^*$ and K or large R), the error is small. This is due to the fact that solutions in this range of parameters consist of very large x' and uniform $S = S_{in}$ covers practically the entire domain. This solution is rather trivial and easily matched by the approximations. As N_g is increased (i.e., increasing $\Delta\rho^*$ and K or decreasing R), the solution takes the form of three regions ($S = S_{in}$, $S = 0$, and $S = 1$), and errors grow due to the inaccuracy of the discontinuity curves [see Fig. 5(d)]. It is apparent that errors for the analytical solution grow much more rapidly than for the SJ model in this range since the

concave discontinuity curves are estimated much more accurately by the latter. The analytical solution reaches a point of local maximum error as the discontinuities present maximum curvature. Then, discontinuities begin a transition from concave to convex shape, which leads to a reduction in error of E and a sharp increase in error of E_{SJ} . A local minimum for E is reached when the discontinuities are linear [e.g., Fig. 5(b)]. As N_g become very large and x' is very small, both E and E_{SJ} grow. This is mainly due to the small region ($\tilde{x} < x'$) that is considered in error calculations [see Eq. (36)] so that, essentially, only erroneous grid blocks on discontinuity curves are included.

Figure 8(f) presents errors for varying n . The general trend is somewhat similar to that in Fig. 8(c) with the increase in error for smallest n values (when x' is small) and the decrease in error for largest n (when solution tends to uniform $S = S_{in}$). The errors in between are related to the curvature of the discontinuities with a minimum for the analytical solution when the curvature is zero ($n \simeq 2$). The main difference from the figures discussed previously is that n has a more pronounced impact on the curvature of the discontinuities leading to very large errors for E , surpassing values of 0.1. As a result, for large n , it is highly

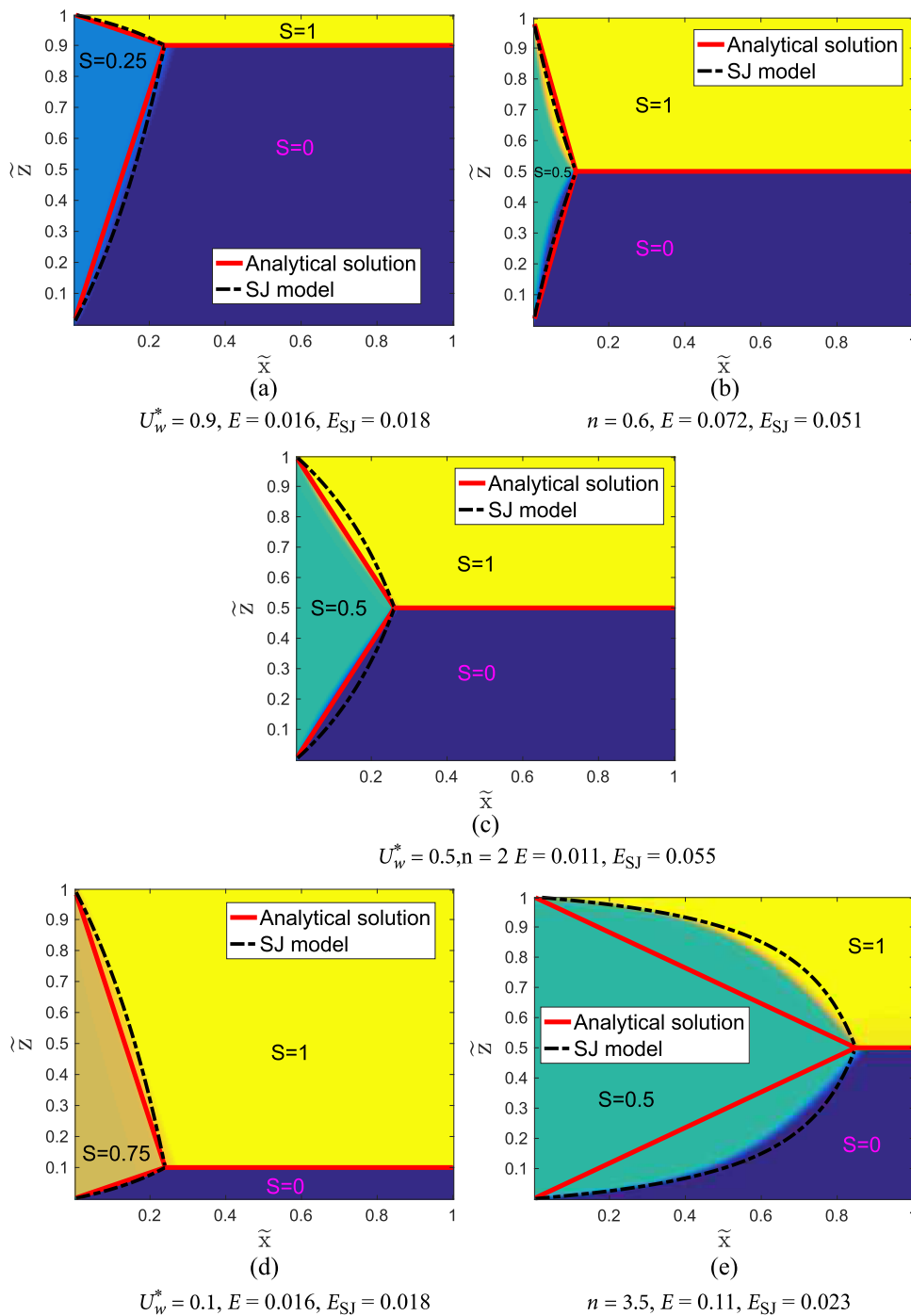


FIG. 7. Two-dimensional saturation solution for numerical simulations (colored areas), analytical solution, and the SJ formula. Different values of U_w^* are considered in (a),(c), and (d), while varying values of n are shown in (b), (c), and (e), specified below each plot.

advantageous to use the SJ formula rather than the analytical solution. We note that different relative permeability models were not tested; however, we expect the behavior of different models to be similar to those discussed above since any monotonic k_r curves with large convex curvature should approximately correspond to large n .

Curves with large concave structures should approximately correspond to small n , and curves with small curvature should be similar to $n \sim 1$.

Substantially different error curve structures are presented in Figs. 8(b) and 8(d). Figure 8(d) is symmetric as expected,

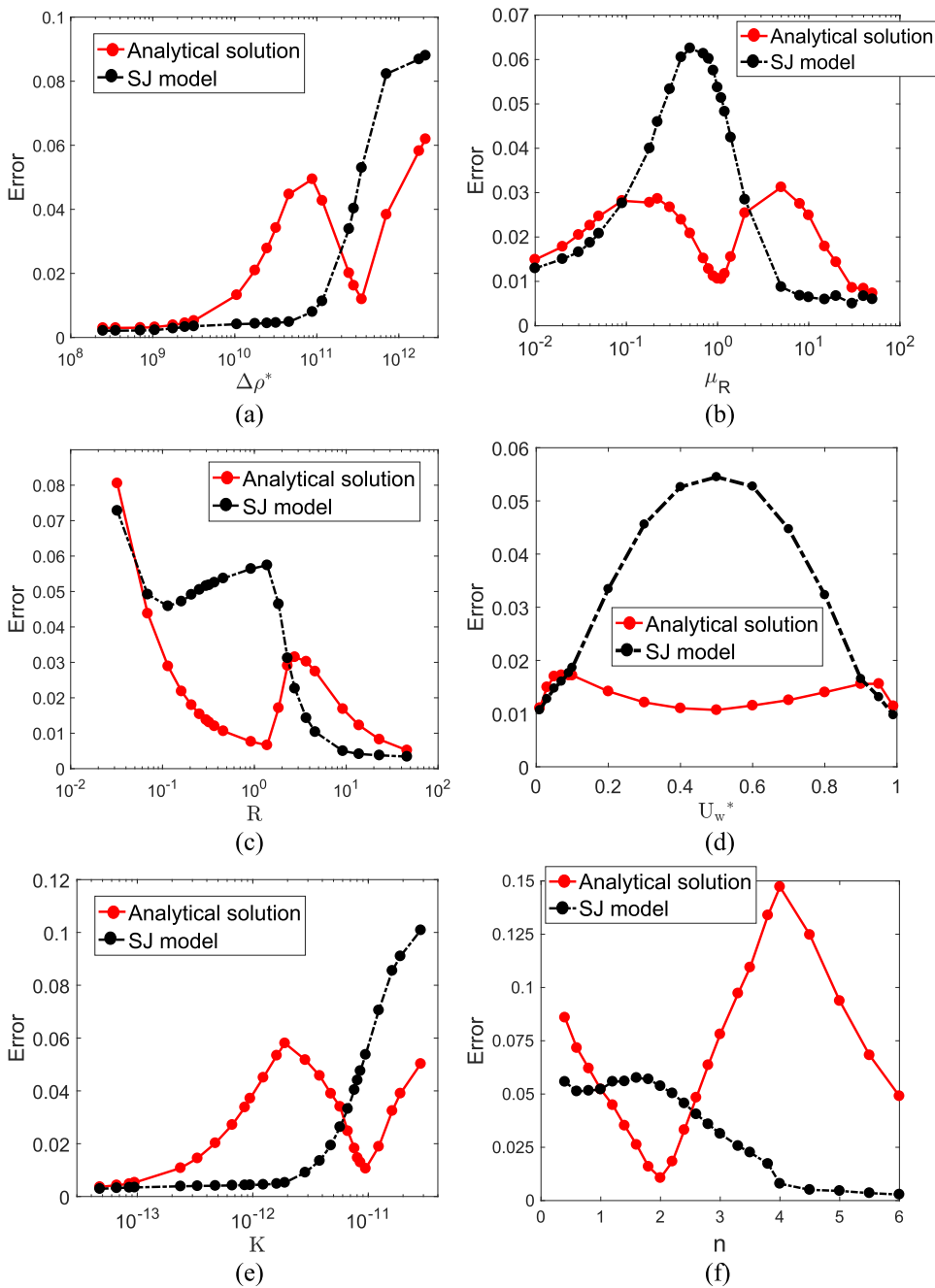


FIG. 8. Errors E and E_{SJ} between approximate and numerical solutions for varying parameters of the full problem [Eq. (3)], as indicated in the axes of plots (a)–(f).

considering the symmetric impact of U_w^* discussed previously regarding Fig. 7. Varying U_w^* does not significantly change x' or the curvature of the discontinuity curves, and therefore, the analytical solution error is fairly constant. It is also small since base case parameters lead to small errors. The SJ model error, on the other hand, has some variation with a maximum error for $U_w^* = 0$ when the discontinuity curves are equal in length. Figure 8(b) shows error for varying μ_R . A minimum in analytical solution error and a maximum

in the SJ model error are obtained for $\mu_R = 1$ when the discontinuity curves are linear. For larger μ_R , the error increases for E and decreases for E_{SJ} as the discontinuity curves become concave, and finally, for even larger μ_R , both errors decrease as the solution tends to one of uniform $S = S_{im}$. For $\mu_R < 1$, E increases as the discontinuities become convex; however, E_{SJ} decreases as the curves become unequal in length. Even for very small μ_R , the errors continue to be decreasing despite $x' \rightarrow 0$, which is contradictory to small values of

R or n in Figs. 8(c) and 8(f). The reason is that here, $z' \rightarrow 0$ when $x' \rightarrow 0$, and thus, the long discontinuities curve remains fairly linear, while the short curve becomes negligibly small.

Observing Fig. 8, we can divide the parametric space into regions in which the analytical solution is more accurate and other regions of higher SJ model accuracy. Generally, we find that larger gravity numbers indicate a preference for the analytical solution. We can define threshold parameter values in which $E < E_{SJ}$ for Figs. 8(a), 8(c), and 8(e) as follows: $\Delta\rho^* > 2 \times 10^{11}$, $K > 6 \times 10^{-12}$, and $R < 2.5$ corresponding to a threshold of $N_g \simeq 1-4$. Outside this range, i.e., for $N_g \lesssim 1$, the SJ formula is preferable. Figure 8(b) indicates that for $\mu_R < 2$, the analytical model is more accurate, while for $\mu_R > 2$, the SJ model should be used. Figure 8(f) shows that for a range of $1 < n < 2.7$, the analytical solution is more accurate, while outside this range, the SJ model is a better approximation, particularly for large n . Figure 8(d) does not reveal a range of U_w^* values for a preferred approximation; however, it appears that the large portion of the intermediate values could have smaller error for the analytical solution, while the extreme values closer to 0 and 1 could have smaller error for the SJ model.

VI. SOLUTION IN CYLINDRICAL COORDINATES

The formulation, solution, and results presented so far are in Cartesian coordinates. We now extend the solution derived in

Sec. IV to cylindrical coordinates in order to apply for cases of radial well injection.²⁹ We begin with Eq. (8) in cylindrical coordinates, given by

$$\frac{1}{r} \frac{\partial(ru_r^t)}{\partial r} + \frac{\partial u_z^t}{\partial z} = 0. \tag{37}$$

Assuming negligible vertical velocity $u_z^t \ll u_r^t$ in a similar manner to Eq. (9), we arrive at

$$u_r^t = \frac{Q}{r}, \tag{38}$$

where Q is the flux in the radial direction injected at $r = 0$. Substituting Darcy's law in Eq. (38), we arrive at the expressions for the nonwetting phase radial velocity,

$$u_{nw,r} = \frac{Q}{r(1 + \lambda_w/\lambda_{nw})}, \tag{39}$$

and $u_{nw,z}$ remains the same as in the previous formulation [see Eq. (11)]. Substituting these in the steady state form of Eq. (1) for $j = nw$ and using cylindrical coordinates gives

$$\frac{1}{r} \frac{\partial}{\partial r} \left[\frac{Q}{1+M} \right] + \frac{\partial}{\partial z} \left[\Delta\rho g \frac{k\lambda_w}{1+M} \right] = 0. \tag{40}$$

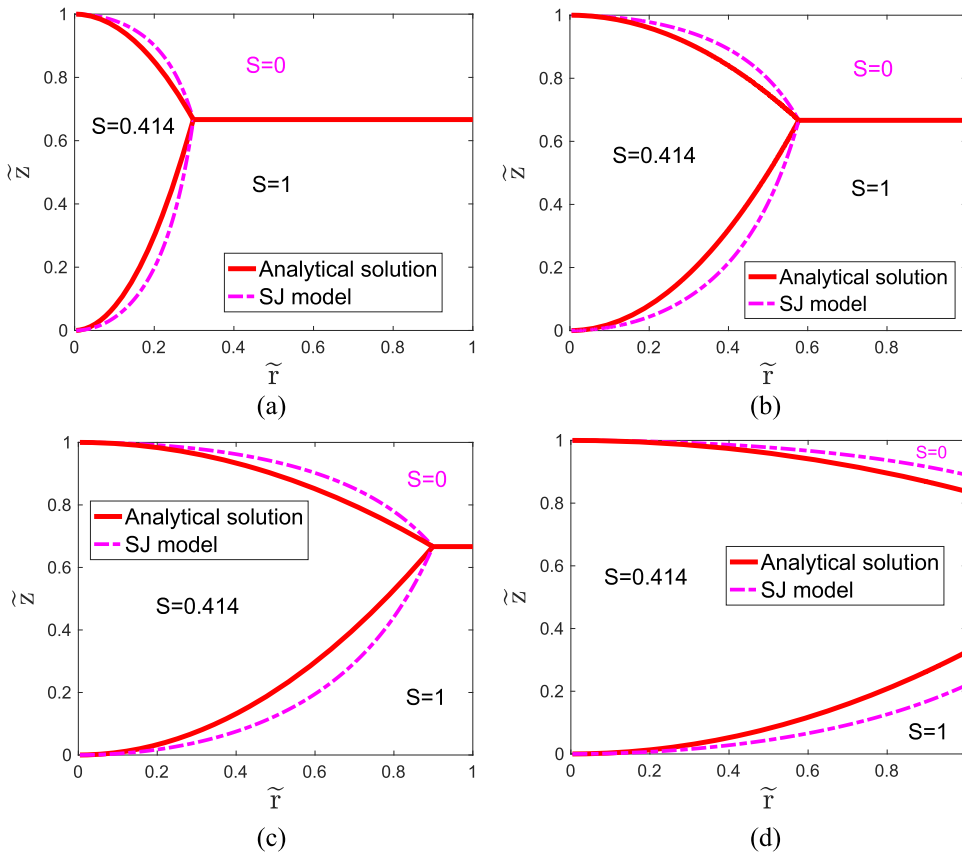


FIG. 9. Two-dimensional saturation solution for the analytical solution and the SJ formula considering radial flow in cylindrical coordinates. Different values of N_g are considered, as indicated below plots (a)–(d).

Using dimensionless parameters $\tilde{z} = z/H$ and $\tilde{r} = r/L$ (L is the radial length of the domain) in Eq. (40), we arrive at

$$\frac{1}{r} \frac{\partial F_1}{\partial \tilde{r}} + \frac{\partial F_2}{\partial \tilde{z}} = 0, \quad (41)$$

where F_1 and F_2 are given by Eq. (14) and $N_g = kL^2 \Delta \rho g / (H \mu_{nw} Q_w)$. Applying the nondimensional coordinate transformation $\zeta = \tilde{r}^2/2$, we arrive at

$$\frac{\partial F_1}{\partial \zeta} + \frac{\partial F_2}{\partial \tilde{z}} = 0, \quad (42)$$

which is the same in structure as the previously derived Eq. (13). The boundary conditions to complete the formulation are given by Eq. (17) and

$$\frac{\lambda_w(S_{in})}{\lambda_{nw}(S_{in})} = Q_w^*, \quad (43)$$

where $Q_w^* = Q_w/Q$ and Q_w is the wetting phase injected at the well ($r = 0$). The segregation height z' is obtained in a similar derivation to Eqs. (19) and (20) to arrive at

$$z' = \frac{1}{\frac{Q_{nw}\mu_{nw}}{Q_w\mu_w} + 1} = \left[\frac{1}{\mu_R} \left(\frac{1}{Q_w^*} - 1 \right) + 1 \right]^{-1}, \quad (44)$$

analogous to Eq. (21).

Equations (42)–(44) are solved in the same manner as described in Sec. IV to obtain $S(\zeta, \tilde{z})$ given by Eq. (34). Then, the inverse transformation is applied to arrive at the solution

$$S(\tilde{r}, \tilde{z}) = \begin{cases} 0, & \{\tilde{r} < \sqrt{2\zeta'} \text{ and } 2\tilde{z}/\tilde{r}^2 < \widehat{D}_1\} \text{ or } \{\tilde{x} > \sqrt{2\zeta'} \text{ and } \tilde{z} < z'\} \\ S_{in}, & \{2\tilde{z}/\tilde{r}^2 > \widehat{D}_1 \text{ and } 2(\tilde{z} - 1)/\tilde{r}^2 < \widehat{D}_2\} \\ 1, & \{\tilde{r} < \sqrt{2\zeta'} \text{ and } 2(\tilde{z} - 1)/\tilde{r}^2 > \widehat{D}_2\} \text{ or} \\ & \{\tilde{r} > \sqrt{2\zeta'} \text{ and } \tilde{z} > z'\}, \end{cases} \quad (45)$$

where ζ' is given by Eq. (31) and \widehat{D}_1 and \widehat{D}_2 are given by Eqs. (32) and (33) with U_w^* replaced by Q_w^* . The solution is presented in Fig. 9, which corresponds to the parameters used in Fig. 5. It is apparent that the discontinuity lines for the analytical solution are no longer linear as in the cartesian case and present concave curvature (for the top curve). Furthermore, the segregation length $r' = \sqrt{2\zeta'}$ is seen to be larger than x' , particularly for larger N_g [Figs. 9(a) and 9(b)].

VII. SUMMARY AND CONCLUSIONS

This work derives approximate equations to two-phase immiscible flow with gravity and viscous effects by implementing a negligible total vertical velocity approach ($u_z^t \approx 0$). The problem considered is of simultaneous injection of two phases, and the solution we seek is the two-dimensional saturation distribution. First, the approximation is tested and shown to have a significant disadvantage due to the violations of mass conservation when injected fluids are of unequal viscosity, i.e., $\mu_w \neq \mu_{nw}$. This is an important finding with implications to previous and future investigations, which utilize the $u_z^t \approx 0$ approximation. Nevertheless, the solution does, in fact, present a wide range of parameters in which $u_z^t \ll u_x^t$, when the approximation should apply. For this reason, we proceed to derive an analytical solution for the approximate equations.

The main advantage of applying the $u_z^t \approx 0$ approximation is that it allows us to derive an analytical solution using the method of characteristics. To overcome mass conservation errors, we apply a correction to the new solution, ensuring conservation. We find that the solution consists of three zones of constant saturation, $S = S_{in}$, $S = 1$, and $S = 0$, separated by linear discontinuity lines. The lines intersect at the point (x', z') , which is the segregation point, when existing within the domain boundaries. The solution for the values of S_{in} , x' , and z' is an exact solution and is in agreement with previous derivations found in the literature. However, the shape of the discontinuity is approximated by the solution and has not been previously discussed.

We carry out a detailed investigation of the new solution accuracy by carrying out comparisons with numerical simulations. Our conclusions are that there is a range of parameters in which the numerical solution does in fact have approximately linear discontinuity curves, and therefore, the analytical solution is accurate. For other cases, a formula presented by Stone⁷ and Jenkins,⁸ which has concave shaped curves (for the top discontinuities), is more accurate. We are able to find threshold values for the six controlling parameters of the problem in which the transition from the analytical solution to the SJ formula occurs. In general, when the point of segregation is closer to the inlet (small \tilde{x}), the analytical solution is preferable, while for cases in which the segregation point is far from the inlet or outside the domain (large \tilde{x}), the SJ formula should be used. A typical threshold value for the transition is found for the gravity number and is given by $N_g \approx 1-4$, where for larger values, the analytical solution is preferred, while for lower values, the SJ model is recommended.

The derived solution is also extended to apply in cases with cylindrical coordinates by using a simple transformation of variables. Overall, the solution could be useful for a range of two-phase flow modeling problems in various applications. Furthermore, linear instability analysis^{30,31} could be applied in the future to investigate the onset of fingers along the discontinuity boundaries.^{32,33} The analytical solution allows immediate calculations for estimating the regions in which fluids and gases will be fully segregated and the mixed region in which they coexist. Using $u_z^t \approx 0$ approximations in more complex problems should be considered cautiously due to the findings here.

NOMENCLATURE

D_1	slope of the discontinuity curve originating at the lower corner of the domain
D_2	slope of the discontinuity curve originating at the upper corner of the domain
D_3	slope of the discontinuity curve between segregated fluid layers
\widehat{D}_j	slope of discontinuity curves after applying correction
E	error between analytical and numerical saturation solutions
E_{SJ}	error between SJ model and numerical saturation solutions
g	gravity, m/s^2
H	domain height, m
K	normalized permeability (k/L^2)
k	absolute permeability, m^2
k_{rj}	relative permeability to phase j

L	domain length, m
M	mobility ratio (λ_w/λ_{nw})
n	Brooks–Corey relative permeability power
N_g	gravity number
p	pressure of both phases
p_j	pressure of phase j, pa
Q	total flux in radial direction at inlet, m ² /s
Q_j	radial flux of phase j at inlet
Q_j^*	normalized radial flux of phase j at inlet (Q_j/Q)
r	radial coordinate, m
r'	\tilde{r} coordinate of the segregation point
\tilde{r}	normalized vertical coordinate
R	normalized domain height (H/L)
S	scaled wetting phase saturation
S_{in}	saturation at inlet boundary
S_J	Stone and Jenkins model
S_j	saturation of phase j
S_{wi}	irreducible wetting phase saturation
t	time, s
U	total horizontal velocity at inlet, m/s
U_j	horizontal velocity of phase j at inlet, m/s
u_j	velocity of phase j, m/s
$u_{j,r}$	radial velocity of phase j, m/s
$u_{j,x}$	horizontal velocity of phase j, m/s
$u_{j,z}$	vertical velocity of phase j, m/s
u^t	total velocity, m/s
u_r^t	radial total velocity, m/s
U_w^*	normalized wetting phase inlet velocity (U_w/U)
u_x^t	horizontal total velocity, m/s
u_z^t	vertical total velocity, m/s
x	horizontal coordinate, m
x'	\tilde{x} coordinate of the segregation point
\tilde{x}	normalized horizontal coordinate
z	vertical coordinate, m
z'	\tilde{z} coordinate of the segregation point
\tilde{z}	normalized vertical coordinate
$\Delta\rho^*$	normalized density difference
$\Delta\rho_j$	phase density difference, kg/m ³
ζ	transformed radial coordinate ($\tilde{r}^2/2$)
ζ'	ζ coordinate of segregation point
λ_j	mobility of phase j
μ_j	viscosity of phase j, pa · s
μ_R	viscosity ratio (μ_w/μ_{nw})
ρ_j	density of phase j, kg/m ³
ϕ	porosity

APPENDIX: INCOMPATIBILITY OF THE $u_z^t = 0$ ASSUMPTION

In this appendix, we show that the assumption $u_z^t = 0$ is incompatible with the full 2D system given by Eq. (3) when viscosities of wetting and non-wetting phases are different, i.e., $\mu_w \neq \mu_{nw}$. Substituting Darcy's moment balance equations for each phase of Eq. (2) into the expression of the zero total vertical velocity assumption ($u_z^t = 0$) yields

$$-\lambda_w \left(\frac{\partial p}{\partial z} + \rho_w g \right) - \lambda_{nw} \left(\frac{\partial p}{\partial z} + \rho_{nw} g \right) = 0. \quad (\text{A1})$$

After rearranging the terms and substituting M , we arrive at

$$\frac{\partial p}{\partial z} + [M(1+M)^{-1} \Delta\rho g + \rho_{nw} g] = 0. \quad (\text{A2})$$

Taking the derivative by x of this results in

$$\frac{\partial}{\partial x} \left[\frac{\partial p}{\partial z} \right] = - \frac{\partial}{\partial x} [M(1+M)^{-1} \Delta\rho g]. \quad (\text{A3})$$

The assumption of $u_z^t = 0$ together with Eq. (8) leads to a constant horizontal velocity [see Eq. (10)] given by

$$U = -k\lambda_{nw}(1+M) \frac{\partial p}{\partial x}. \quad (\text{A4})$$

Taking the derivative by x of this leads to

$$\frac{\partial}{\partial z} \left[\frac{\partial p}{\partial x} \right] = - \frac{U}{k} \frac{\partial}{\partial z} \left[\frac{1}{\lambda_{nw}(1+M)} \right]. \quad (\text{A5})$$

Combining Eqs. (A3) and (A5) results in

$$\frac{\partial}{\partial x} \left[\frac{1}{1+M} \right] + \frac{U}{\Delta\rho k g} \frac{\partial}{\partial z} \left[\frac{1}{\lambda_{nw}(1+M)} \right] = 0, \quad (\text{A6})$$

remembering that $M(1+M)^{-1} = 1 - (1+M)^{-1}$. Substituting Eq. (12) in the first term of Eq. (A6) and integrating in z yields

$$\frac{\lambda_w \lambda_{nw}}{\lambda_w + \lambda_{nw}} + \left(\frac{k \Delta\rho g}{U} \right)^2 \frac{1}{\lambda_w + \lambda_{nw}} = f(x). \quad (\text{A7})$$

Applying boundary condition $S = 0$ at $\tilde{z} = 0$, i.e., $\lambda_{nw}(0) = 0$, $\lambda_w(0) = 1/\mu_w$ leads to

$$f(x) = \mu_w \left(\frac{k \Delta\rho g}{U} \right)^2, \quad (\text{A8})$$

while applying boundary condition $S = 1$ at $\tilde{z} = 1$, i.e., $\lambda_{nw}(1) = 1/\mu_{nw}$, $\lambda_w(1) = 0$ leads to a different expression for $f(x)$ as follows:

$$f(x) = \mu_{nw} \left(\frac{k \Delta\rho g}{U} \right)^2. \quad (\text{A9})$$

The above contradiction between Eqs. (A8) and (A9) shows that the assumption $u_z^t = 0$ and the system of Eq. (3) are compatible only for the case where the phase viscosities are equal.

REFERENCES

- N. M. Ribe, "Theory of melt segregation: A review," *J. Volcan. Geotherm. Res.* **33**, 241–253 (1987).
- The Petroleum System: From Source to Trap*, AAPG Memoir No. 60, edited by L. B. Magoon and W. G. Dow (The American Association of Petroleum Geologists, Tulsa, OK, 1994).
- M. El-Bealy, "Modeling of interdendritic strain and macrosegregation for dendritic solidification processes: Part I. Theory and experiments," *Mettall. Mater. Trans. B* **31**, 331–343 (2000).
- T. Baumgart, A. T. Hammond, P. Sengupta, S. T. Hess, D. A. Holowka, B. A. Baird, and W. W. Webb, "Large-scale fluid/fluid phase separation of proteins and lipids in giant plasma membrane vesicles," *Proc. Natl. Acad. Sci. U. S. A.* **104**, 3165–3170 (2007).
- A. Rogerson and E. Meiburg, "Numerical simulation of miscible displacement processes in porous media flows under gravity," *Phys. Fluids A* **5**, 2644–2660 (1993).
- A. Riaz and H. A. Tchelepi, "Numerical simulation of immiscible two-phase flow in porous media," *Phys. Fluids* **18**, 014104 (2006).

- ⁷H. L. Stone, "Vertical conformance in an alternating water-miscible gas flood," SPE Annual Technical Conference and Exhibition, Society of Petroleum Engineers (SPE 11130), 1982.
- ⁸M. K. Jenkins, "An analytical model for water/gas miscible displacements," in *SPE Enhanced Oil Recovery Symposium* (Society of Petroleum Engineers, 1984).
- ⁹W. R. Rossen and C. J. Van Duijn, "Gravity segregation in steady-state horizontal flow in homogeneous reservoirs," *J. Pet. Sci. Eng.* **43**, 99–111 (2004).
- ¹⁰R. Farajzadeh, A. Andrianov, R. Krastev, G. J. Hirasaki, and W. R. Rossen, "Foam-oil interaction in porous media: Implications for foam assisted enhanced oil recovery," *Adv. Colloid Interface Sci.* **183–184**, 1–13 (2012).
- ¹¹J. M. van der Meer, R. Farajzadeh, W. R. Rossen, and J. D. Jansen, "Influence of foam on the stability characteristics of immiscible flow in porous media," *Phys. Fluids* **30**, 014106 (2018).
- ¹²J. Ma, X. Wang, R. Gao, F. Zeng, C. Huang, P. Tontiwachwuthikul, and Z. Liang, "Study of cyclic CO₂ injection for low-pressure light oil recovery under reservoir conditions," *Fuel* **174**, 296–306 (2016).
- ¹³C.-W. Kuo and S. M. Benson, "Analytical study of effects of flow rate, capillarity, and gravity on co/brine multiphase-flow system in horizontal corefloods," *SPE J.* **18**, 708–720 (2013).
- ¹⁴J. A. Neufeld and H. E. Huppert, "Modelling carbon dioxide sequestration in layered strata," *J. Fluid Mech.* **625**, 353–370 (2009).
- ¹⁵H. Liu, Y. Zhang, and A. J. Valocchi, "Lattice Boltzmann simulation of immiscible fluid displacement in porous media: Homogeneous versus heterogeneous pore network," *Phys. Fluids* **27**, 052103 (2015).
- ¹⁶A. Rabinovich, "Analytical corrections to core relative permeability for low-flow-rate simulation," *SPE J.* **23**, 1851 (2018).
- ¹⁷M. Jamshidnezhad and T. Ghazvian, "Analytical modeling for gravity segregation in gas improved oil recovery of tilted reservoirs," *Transp. Porous Media* **86**, 695–704 (2011).
- ¹⁸M. Izadi and S. Kam, "Investigating supercritical CO₂ foam propagation distance: Conversion from strong foam to weak foam vs. gravity segregation," *Transp. Porous Media* **131**, 223–250 (2018).
- ¹⁹M. J. Shojaei, K. Osei-Bonsu, P. Grassia, and N. Shokri, "Foam flow investigation in 3D-printed porous media: Fingering and gravitational effects," *Ind. Eng. Chem. Res.* **57**, 7275–7281 (2018).
- ²⁰W. R. Rossen, C. J. Van Duijn, Q. P. Nguyen, C. Shen, and A. K. Vikingstad, "Injection strategies to overcome gravity segregation in simultaneous gas and water injection into homogeneous reservoirs," *SPE J.* **15**, 76–90 (2010).
- ²¹D. Zhou, F. J. Fayers, and F. M. Orr, Jr., "Scaling of multiphase flow in simple heterogeneous porous media," *SPE Reservoir Eng.* **12**, 173–178 (1997).
- ²²A. Rabinovich, E. Anto-Darkwah, and A. M. Mishra, "Determining characteristic relative permeability from coreflooding experiments: A simplified model approach," *Water Resour. Res.* **55**, 8666–8690, <https://doi.org/10.1029/2019-wr025156> (2019).
- ²³R. H. Brooks and A. T. Corey, "Properties of porous media affecting fluid flow," *J. Irrig. Drain. Div.* **92**, 61–90 (1966).
- ²⁴S. E. Buckley and M. C. Leverett, "Mechanism of fluid displacement in sands," *Trans. AIME* **146**, 107–116 (1942).
- ²⁵H. Cao, "Development of techniques for general purpose simulators," Ph.D. thesis, Stanford University, Stanford, CA, USA, 2002.
- ²⁶P. Bedrikovetsky, *Mathematical Theory of Oil and Gas Recovery: With Applications to EX-USSR Oil and Gas Fields* (Springer Science & Business Media, 2013), Vol. 4.
- ²⁷P. D. Lax, "Hyperbolic systems of conservation laws II," *Commun. Pure Appl. Math.* **10**, 537–566 (1957).
- ²⁸R. Courant and K. O. Friedrichs, *Supersonic Flow and Shock Waves* (Springer Science & Business Media, 1999), Vol. 21.
- ²⁹A. Rabinovich, "An analytical solution for cyclic flow of two immiscible phases," *J. Hydrol.* **570**, 682–691 (2019).
- ³⁰L. T. Hoang, A. Ibragimov, and T. T. Kieu, "A family of steady two-phase generalized forchheimer flows and their linear stability analysis," *J. Math. Phys.* **55**, 123101 (2014).
- ³¹C. Gin and P. Daripa, "Stability results for multi-layer radial hele-shaw and porous media flows," *Phys. Fluids* **27**, 012101 (2015).
- ³²G. M. Homsy, "Viscous fingering in porous media," *Annu. Rev. Fluid Mech.* **19**, 271–311 (1987).
- ³³M. C. Kim, "Linear stability analysis on the onset of the viscous fingering of a miscible slice in a porous medium," *Adv. Water Resour.* **35**, 1–9 (2012).